Magnetic Analysis of Switched Reluctance Actuators in Levitated Linear Transporters

Zhen Gang Sun, *Student Member, IEEE*, Norbert C. Cheung, *Senior Member, IEEE*, Shi Wei Zhao, *Member, IEEE*, and Wai-Chuen Gan, *Senior Member, IEEE*

***Abstract*—A novel linear magnetic levitated actuator using the switched reluctance principle is addressed in this paper. This actuator can be applied to precise motion control of automation machines. The proposed system has the advantages of a simple and robust structure, and direct drive capability. The contactless structure eliminates mechanical wear, friction, noise, and heat generation. To verify the feasibility of the proposed system, the magnetic levitated force is analyzed by magnetic circuit analysis (MCA) and by finite-element analysis (FEA). A prototype structure is fabricated, and experiments are performed with the actual hardware. Results of the MCA and the FEA are both compared with the results obtained from the hardware experiments. They all agree with the proposed design methodology. This paper can form a useful reference in the design of a mechanical structure for magnetic levitated switched reluctance actuators.**

***Index Terms*—Electromagnetic force, finite-element analysis (FEA), linear switched reluctance actuator, magnetic circuit analysis (MCA), magnetic levitation.**

I. Introduction

MAGNETIC levitated actuators and magnetic levitated transportation systems have been actively studied by worldwide researchers, due to the advantages of reduced moving mechanical components and lower maintenance cost. Common forms of magnetic levitated motion systems include the following: 1) the short rotor linear induction motor with lateral stabilization [1], [2]; 2) the permanent-magnet (PM) motor with a magnetic bearing system [3]–[5]; and 3) the PM linear track with high-temperature superconductor support [6]. These magnetic levitated schemes are both effective and efficient, but their motor structure is complex, and their manufacturing costs are expensive. In addition, permanent magnets have highly temperature-dependent characteristics [7], and the employment of high-temperature superconductors in the motors creates manufacturing and maintenance problems. The aforementioned actuators are targeted for high-speed mass transportation systems.

Manuscript received March 4, 2010; revised June 11, 2010 and July 19, 2010; accepted August 30, 2010. Date of publication September 7, 2010; date of current version November 12, 2010. This work was supported in part by the University Grants Council under Project PolyU 5141/05E and in part by the Hong Kong Polytechnic University under Project G-YX2Q. The review of this paper was coordinated by Prof. J. Hur.

Z. G. Sun, N. C. Cheung, and S. W. Zhao are with the Department of Electrical Engineering, Hong Kong Polytechnic University, Kowloon, Hong Kong (e-mail: norbert.cheung@polyu.edu.hk).

W.-C. Gan is with the R&D Motion, ASM Assembly Automation Ltd., Kwai Chung, N.T., Hong Kong.

Digital Object Identifier 10.1109/TVT.2010.2073727

In this paper, a novel magnetic levitated switched reluctance linear actuator is proposed. The actuator is designed for applications in small- to medium-scale automation machinery. The linear actuator has a simple and robust structure and is suitable for high-speed and high-precision position control with direct drive capability. The proposed actuator can be operated under harsh environments over a wide temperature range. The magnetic levitation and motion force are produced by the switched reluctance principle. A switched reluctance actuator has a comparable efficiency and a slightly less force-to-mass ratio than a permanent magnet actuator. However, it has a simple and robust structure, and it does not contain a permanent magnet to reduce cost [8], [9]. These make the switched reluctance actuation a potential candidate for high-reliability operation in a harsh environment.

The reason that the switched reluctance motor (SRM) has not been widely used in magnetic levitated systems is because of its inherent complex flux characteristics. SRM derives its force from the change of flux, and flux exhibits a complex and nonlinear behavior. Therefore, it is difficult to design a magnetic levitated linear SRM. To validate the design of the magnetic levitated actuator, a comprehensive levitation force analysis of the actuator is required. Generally, there are two techniques that can be used to analyze force in the design of SRMs. The two methods are referred to as magnetic circuit analysis (MCA) [10]–[15] and finite-element analysis (FEA) [16]–[22]. MCA is simple and highly efficient in computation, but its accuracy mostly depends on the choice of magnetic flux paths. FEA is accurate in calculation by spatial discretization, but it is computational intensive and very time consuming [12].

The method for analytical estimation of the permeance of flux paths is discussed in [10], and the flux path models of several type of structures of high-permeability material are built and analyzed. The permeance model and the reluctance force between the tooth structures of motors are developed in [11], and three different translator position regions are considered to evaluate the permeance through the air gap during the motion of the translator. On the basis of the preceding flux path models, numerous permeance models and their corresponding MCA methods are developed and employed in the design and analysis of different structures of SRMs. In [12], four different translator position regions are used to calculate the permeance in the air gap of a linear SRM (LSRM). In [13], permeance models in five different translator position regions are built to evaluate the propulsion force of a double-sided double-translator LSRM. In [14], inductances and flux linkages for three identified rotor position regions of rotary SRM are computed to verify the

design of the motor. A high-speed magnetic circuit network is approached as the calculation tool for electromechanical actuator design [15]; this method is effective and solves within a much shorter time, compared with the FEA method.

The FEA method is also widely implemented to design and analyze electromechanical devices. In [16], different physical sizes of SRMs are compared by using a 2-D FEA model. In [17], the flux linkage and force of an electromechanical valve actuator are simulated by a 3-D FEA model. A 3-D FEA model of rotary SRMs is developed to simulate the motor in many different rotor positions in [18]. The force and torque computation of SRMs are compared by a 2-D FEA model and a 3-D FEA model in [19], and the results show that the accuracy of the 3-D model is better than that of the 2-D model. The FEA method based on Maxwell stress is used to predict the electromagnetic vibration in [20]. The FEA method on the basis of the virtual work principle is presented to solve the electromagnetic force in [21]. In [22], the preceding two FEA methods, i.e., the Maxwell stress method and the virtual work method, are proposed for electromagnetic torque computation, and the advantages of each method are concluded.

In this paper, both the MCA model and the 3-D FEA model are used to analyze magnetic levitation force, and the simulated results are compared with the actual measurement of the prototype hardware to confirm the feasibility of the proposed actuator.

The organization of this paper is given as follows: The design of the magnetic levitated linear switched reluctance actuator is discussed in Section II. In Section III, an MCA model is constructed to calculate the magnetic levitation force. In Section IV, an FEA model is developed and implemented to simulate the magnetic levitation force. Then, the force measurements of the actual prototype hardware are performed, and the results are compared with the MCA and FEA results in Section V. Finally, some concluding remarks are given in Section VI.

II. Magnetic Levitated Linear Switched Reluctance Actuator

Fig. 1 shows the 3-D schematic diagram of the magnetic levitated linear transporter, and Fig. 2 shows the 2-D schematic diagram of the switched reluctance actuator. Fig. 3 shows the actual appearance of the magnetic levitated linear transporter. The actuator is driven by three propulsion coils and four levitation coils separately located on each corner of the moving platform.

The body and the moving platform of the magnetic levitated linear transporter are manufactured using lightweight aluminum so that the total weight of the transporter and the inertia of the moving platform are low. The track guide and the core of the windings are laminated with 0.5-mm silicon steel plates. All the laminated plates are produced using a standard press tool. Four proximity analog position sensors are located on the four corners of the moving platform to measure air gap between the moving platform and the track rails and to provide the feedback position to implement the levitation operation. The propulsion track has a tooth structure rail track, with three separate coils to provide the desired horizontal forces [23]. The levitation track, on the other hand, has a smooth profile, and it provides the lifting forces to the moving platform.

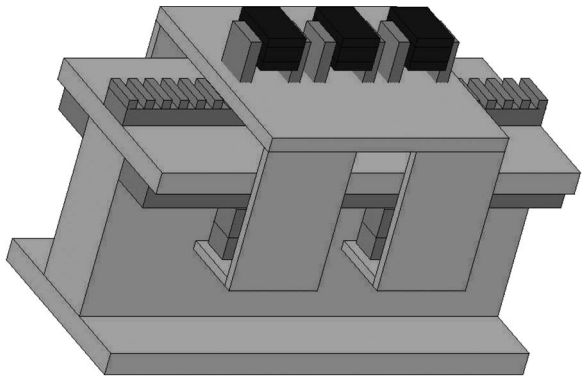

Fig. 1. Schematic of the magnetic levitated linear transporter.

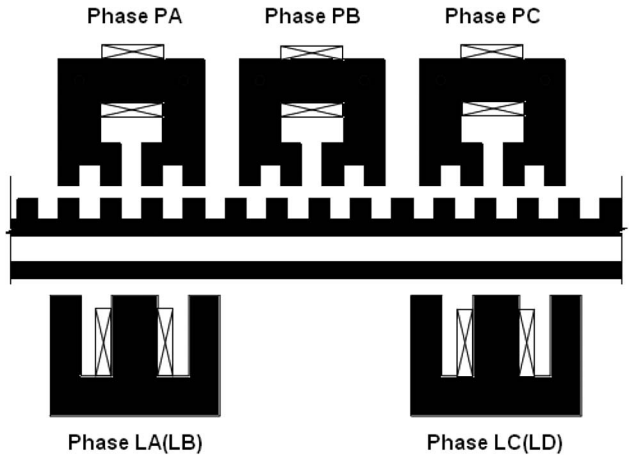

Fig. 2. Schematic of the switched reluctance actuator.

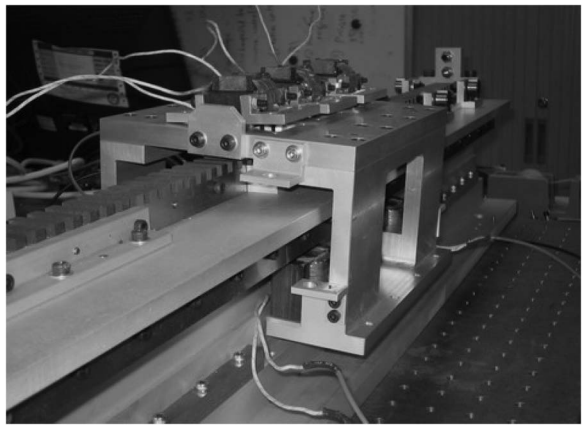

Fig. 3. Prototype of the proposed magnetic levitated linear transporter.

Since the moving platform runs on a straight line, there is no need to install guidance coils to compensate for the lateral forces. However, the normal force produced by the three propulsion coils needs to be compensated for two reasons: 1) The direction of normal force is downward, and 2) the normal force could rotate the moving platform. From Fig. 2, if the phase PA of propulsion coils is excited, the normal force will rotate the moving platform counterclockwise, and hence, the

TABLE I
MOTION DESIGN SPECIFICATIONS

Mass of the platform	3kg
Maximum loading	3kg
Maximum acceleration	10m/s^2
Maximum velocity	1m/s
Maximum force	60N
Peak power of the motor	60W
Position accuracy	10μm

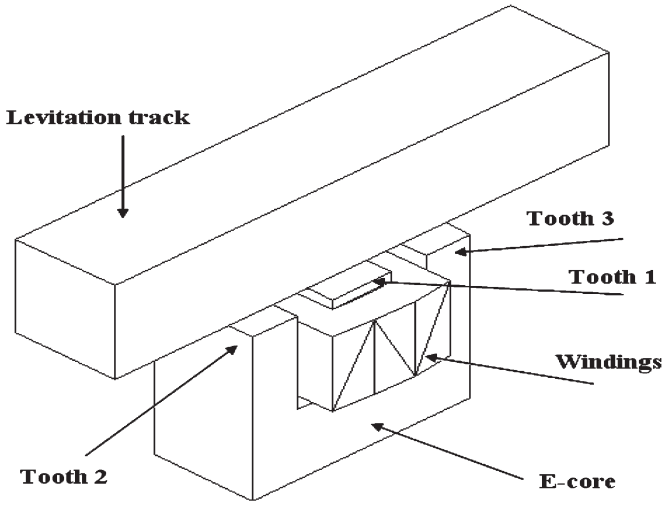

Fig. 4. Schematic of the single-levitation-coil model.

TABLE II
PARAMETERS OF THE SINGLE LEVITATION COIL

Symbol	Definition	Value
Wtp2, Wtp3	Width of tooth 2 and 3 separately	9mm
Wtp1	Width of tooth 1	12mm
h	Tooth height	20mm
d	Tooth depth	20mm
W12	Width between tooth 1 and 2	9mm
W13	Width between tooth 1 and 3	9mm
l	Yoke height	15mm
D	Track depth	20mm
H	Track height	20mm
N	Number of coil turns	30

phase LA and LB of levitation coils are excited to compensate the normal force. In the same measure, the rotation effect of normal force from phase PC can be counteracted by phase LC and LD excitation. Due to the geometrical symmetry, the normal force by phase PB will be in self-symmetry around the mass center of the moving platform; in this case, the torque moment can be reasonably ignored. The motion specifications of the proposed levitated system are listed in Table I.

The levitation actuator is assembled in E-shape to ease the mass production. The schematic of a single levitation coil is shown in Fig. 4. The four levitation coils are with of the same dimensions; therefore, the analysis of one coil is sufficient for the analysis of the actuator. The parameters of the single levitation coil are listed in Table II.

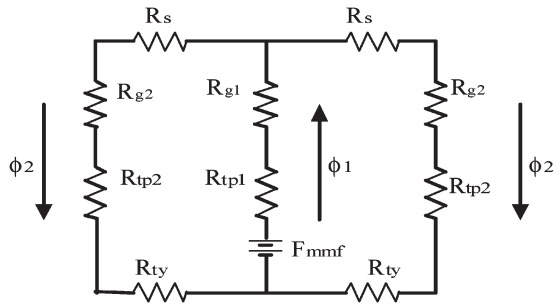

Fig. 5. Magnetic equivalent circuit diagram.

III. MAGNETIC CIRCUIT ANALYSIS MODELING

Fig. 5 shows the magnetic equivalent circuit diagram of the single levitation coil.

A. Levitation Force

The magnetomotive force equation can be written by using Ampere's circuital law, i.e.,

$$F_{\mathrm{mmf}} = Ni = \phi_1 R_{g1} + \phi_2 R_{g2} + H_s l_s + H_{tp1} l_{tp1} + H_{tp2} l_{tp2} + H_{ty} l_{ty} \quad (1)$$

where F_{mmf} denotes the total magnetomotive force (mmf) source, N denotes the number of coil turns, i denotes the exciting current, Φ denotes the flux, R_g denotes the air gap reluctance, $R_g = 1/P$, P is the air gap permeance, H denotes the magnetic field intensity, and l denotes the flux path length.

Table II shows that the width between adjacent teeth is 9 mm, whereas the air gap does not exceed 2 mm. Therefore, the flux due to leakage between adjacent teeth is small, and the leakage flux could be neglected; then, the flux $\Phi_1 = 2\Phi_2$ because of the symmetry of the E core.

The flux density B is given by

$$B = \frac{\phi}{A} \quad (2)$$

where A denotes the cross-sectional area of the flux path.

The magnetic field intensity H can be obtained from the flux density versus magnetic field intensity (B-H) characteristics curve of silicon steel.

Due to the nonlinearity of the B-H characteristics, an iterative procedure is adopted to calculate the flux Φ. A bisection root-finding algorithm [12] is introduced by assuming an arbitrary initial value of Φ. However, the value of flux density B is limited in the B-H characteristics curve. Hence, the initial value Φ cannot be arbitrary large; otherwise, the interpolation calculation will be difficult. Assume that the total F_{mmf} is used up in the air gap. Then, the extreme value of the flux can be obtained from (1) by omitting ΣHl. Therefore, the initial maximum value of the flux Φ_1 can be supposed as

$$\phi_{1\max} \le \phi_{\mathrm{ext}} = \frac{2Ni}{2R_{g1} + R_{g2}}. \quad (3)$$

The error between the right-hand and left-hand sides of (1) can be used to test for convergence. The flowchart for the

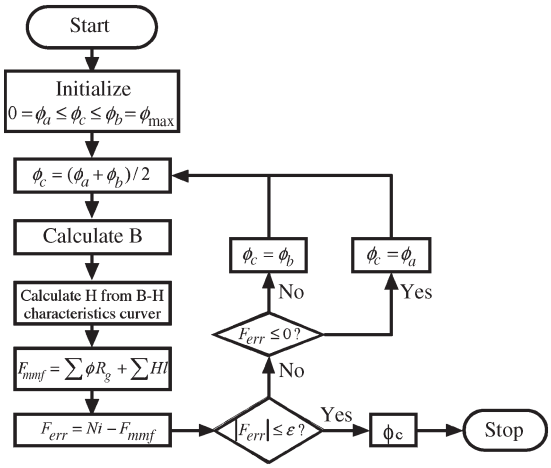

Fig. 6. Flow chart of the iterative procedure for calculating the flux.

iterative procedure is shown in Fig. 6, and the suggested value for error in the iterative procedure is $\varepsilon = 0.0001$.

The levitation force can be calculated by using the principle of conservation of energy, i.e.,

$$dW_{\text{elec}} = dW_{\text{store}} + dW_{\text{mech}} + dW_{\text{loss}} \tag{4}$$

where dW_{elec} is the incremental electric input energy; dW_{store} is the incremental stored magnetic energy; dW_{mech} is the incremental mechanical energy; and dW_{loss} is the incremental loss energy, which includes the energy dissipation in the resistance of the exciting coil and energy loss, owing to hysteresis effects in the silicon steel.

Due to the low resistance of the exciting coil ($R = 0.3\ \Omega$) and the low hysteresis loss of silicon steel, the dW_{loss} term can be deleted to simplify the calculation, i.e.,

$$f_z \cdot dz = dW_{\text{mech}} = dW_{\text{elec}} - dW_{\text{store}} = dW'_{\phi} \tag{5}$$

$$f_z = \frac{dW'_{\phi}}{dz} = \frac{\int_0^F \phi_z dF - \int_0^F \phi_{z+dz} dF}{dz} \tag{6}$$

where f_z denotes the levitation force, dz denotes a very small change of the air gap, and dW'_{ϕ} denotes the incremental coenergy in the magnetic field.

B. Air Gap Permeance

Once the air gap permeance is known, the iterative solution gives the value of flux; therefore, the levitation force can be deduced from (6). The air gap permeance can be determined by selecting suitable flux paths. In this paper, the air gap permeance model used is based on [10] and [12]. The air gap has seven different types of flux paths to estimate air gap permeance, as shown in Fig. 7.

The derived air gap permeances are given here, corresponding to each flux path.

Path 1 is the basic parallelepiped geometry, i.e.,

$$P_{j1} = \mu_0 \frac{W_{tpj} d}{z}. \tag{7}$$

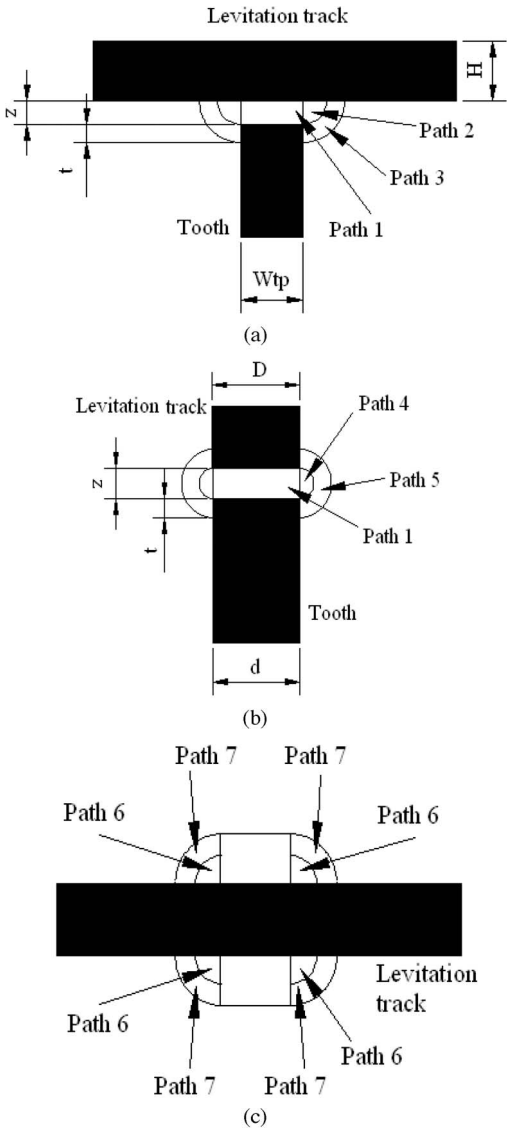

Fig. 7. Schematic of flux paths within air gap. (a) Front view. (b) Side view. (c) Top view.

Path 2 is a quarter-circular cylinder geometry, i.e.,

$$P_{j2} = \mu_0 \frac{\frac{1}{4}\pi z^2 d / 1.211z}{1.211z} = 0.535 \mu_0 d. \tag{8}$$

Path 3 is a quarter annulus geometry, i.e.,

$$P_{j3} = \int_z^{z+t} \mu_0 \frac{d}{\pi r/2} dr = 0.637 \mu_0 d \ln\left(1 + \frac{t}{z}\right). \tag{9}$$

Path 4 is a semicircular cylinder geometry, i.e.,

$$P_{j4} = \mu_0 \frac{\frac{1}{2}\pi \left(\frac{z}{2}\right)^2 W_{tpj} / 1.211z}{1.211z} = 0.268 \mu_0 W_{tpj}. \tag{10}$$

Path 5 is a half annulus geometry, i.e.,

$$P_{j5} = \int_{z/2}^{t+z/2} \mu_0 \frac{W_{tpj}}{\pi r} dr = 0.318 \mu_0 W_{tpj} \ln\left(1 + \frac{2t}{z}\right). \tag{11}$$

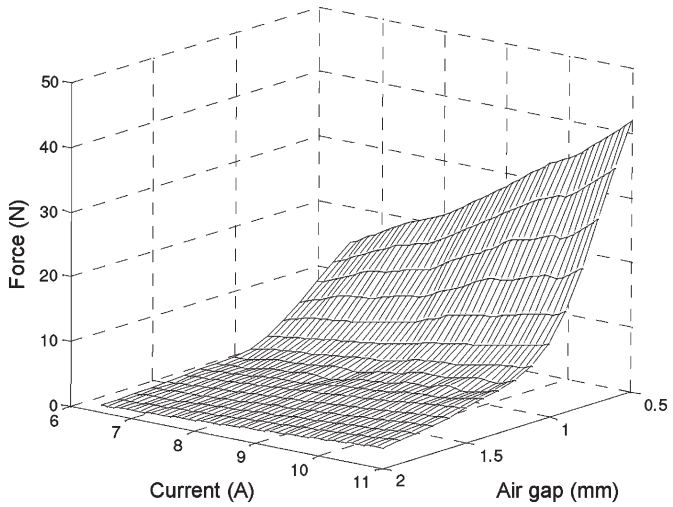

Fig. 8. MCA force–current–position 3-D chart.

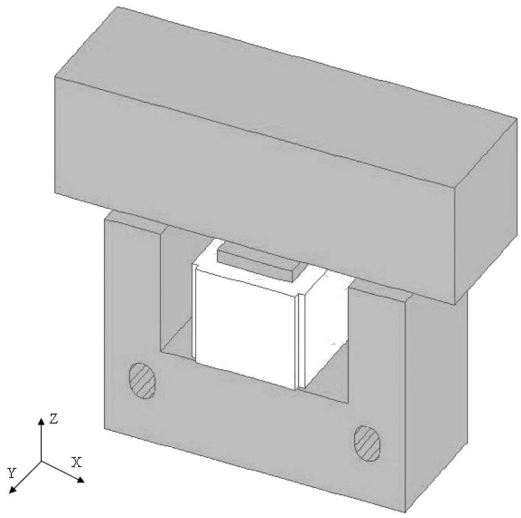

Fig. 9. 3-D FEA model.

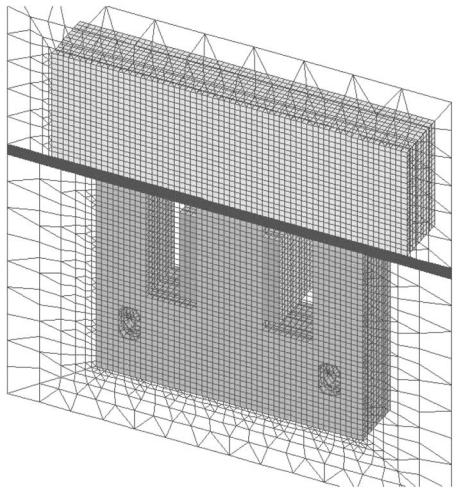

Fig. 10. Cross section of 3-D meshes.

Path 6 is a spherical quadrant geometry, i.e.,

$$P_{j6} = \mu_0 \frac{\frac{1}{8} \times \frac{4}{3}\pi z^3 / 1.311z}{1.311z} = 0.304\mu_0 z. \tag{12}$$

Path 7 is a spherical shell quadrant geometry, i.e.,

$$P_{j7} = \mu_0 \frac{1}{2} \frac{\pi/2(z + t/2)t}{\pi/2(z + t/2)} = 0.5\mu_0 t \tag{13}$$

where $j = 1$ or 2 denotes tooth 1 and tooth 2, respectively; μ_0 is the permeability of air; W_{tp} is the width of tooth; d is the tooth depth; and h is the tooth height $t = h/12$.

The flux of each path can be calculated by the combination of (1) and (7)–(13). Then, the levitation forces are obtained by using (6). Fig. 8 shows the MCA force–current–position 3-D chart.

IV. Finite-Element Analysis Modeling

In general, FEA provides more accurate results than the magnetic equivalent circuit approach since it considers a large number of flux paths, compared with the MCA method. To fully characterize the proposed levitation system and verify the accuracy of the analytical MCA method, 3-D FEA models are built by using the MEGA software. This software can be used to model any device that can be described in terms of Maxwell's equations. The use of 3-D finite elements by MEGA software in SRM and other electrical machines design have been discussed in [24] and [25].

Fig. 9 shows the 3-D FEA model, and Fig. 10 shows the cross section of 3-D meshes. The 3-D model is built by extruding a base plane (X-Z plane) along its perpendicular axis (Y-axis). A base is first constructed in the X-Z plane as a 2-D framework of nodes and elements. This structure consists of triangles and quadrilaterals, with each edge defined by two nodes. The field distribution is the key factor that affects the distribution of finite elements. Where the rate of change of field is greater, the elements should be fine enough; otherwise, the answers at these nodes will not be accurate. After the 2-D model is set up, a 3-D mesh can be created level by level from the base plane. The model contains sufficient detail to define all the changes that occur along the Y-axis direction to form a series of similar-spaced planes having similar discretization. The type of "race track" winding is chosen from a variety of coils in the software library. The winding is "wound" on the levitation tooth, and current distribution is uniform over the entire coil cross-sectional space. Although meshing is not needed for winding, it should be embedded as reduced scalar elements, and the region where the finite elements reside this winding should be represented as a "reduced scalar potential" ϕ. Then, the magnetic field due to the source current is derived from Biot-Savart law [26] as

$$H_s = -\frac{1}{4\pi} \int_v J_s \times \nabla \left(\frac{1}{r} \right) dV \tag{14}$$

where r is the distance between the current source point where the field is calculated, J_s is the source current density, and V is the current-carrying volume.

The actual field is the sum of source field H_s and the gradient of ϕ, i.e.,

$$H = -\nabla\phi + H_s. \tag{15}$$

After the 3-D model is meshed and the winding is defined, normal flux or tangential flux boundary conditions can be set for planes of symmetry, and the next step is to solve the problems.

It can be seen from Fig. 10 that the number of nodes in the air gap is very large, which means that the elements in the air gap are pretty fine. These meshes are based on the following criterion: The air gap predominantly determines the flux distribution as most of the mmf, and hence, the magnetic energy is applied to the air gap as long as the core is not saturated. This will guarantee the accuracy of the FEA model.

With modifying the air gap and the exciting currents, the levitation forces for various exciting currents and air gap can be obtained. The simulation takes into account the cases where air gap positions change from 0.5 to 2 mm, and exciting currents change from 6.5 to 11 A. The flux contours are shown in Fig. 11. Note that the values of the numeric bar in each figure are different. The values in Fig. 11(a) ($z = 0.5$ mm, $i = 6.5$ A) are lower than those in Fig. 11(b) ($z = 0.5$ mm, $i = 11$ A) but higher than those in Fig. 11(c) ($z = 2$ mm, $i = 6.5$ A). Values in Fig. 11(d) ($z = 2$ mm, $i = 11$ A) are lower than those in Fig. 11(b) ($z = 0.5$ mm, $i = 11$ A) but higher than those in Fig. 11(c) ($z = 2$ mm, $i = 6.5$ A).

By comparing the flux contours in Fig. 11(a) ($z = 0.5$ mm, $i = 6.5$ A) with those in Fig. 11(b) ($z = 0.5$ mm, $i = 11$ A) or comparing Fig. 11(c) ($z = 2$ mm, $i = 6.5$ A) with Fig. 11(d) ($z = 2$ mm, $i = 11$ A), the results show that the higher the exciting current, the relatively higher the levels of flux. By comparing the flux contours in Fig. 11(a) ($z = 0.5$ mm, $i = 6.5$ A) with those in Fig. 11(c) ($z = 2$ mm, $i = 6.5$ A) or comparing Fig. 11(b) ($z = 0.5$ mm, $i = 115$ A) with Fig. 11(d) ($z = 2$ mm, $i = 11$ A), the results show that the larger air gap position, the higher reluctance flux paths and, hence, relatively lower levels of flux. All those results accord with the mmf equation (1), which indicates that the function between the flux Φ and the exciting current i is monotone increasing, and the function between the flux Φ and the air gap reluctance R_g is monotone decreasing.

Fig. 12 shows the FEA force–current–position 3-D chart. As shown in Figs. 8 and 12, the force variation trend of the FEA model is similar to that of the MCA model.

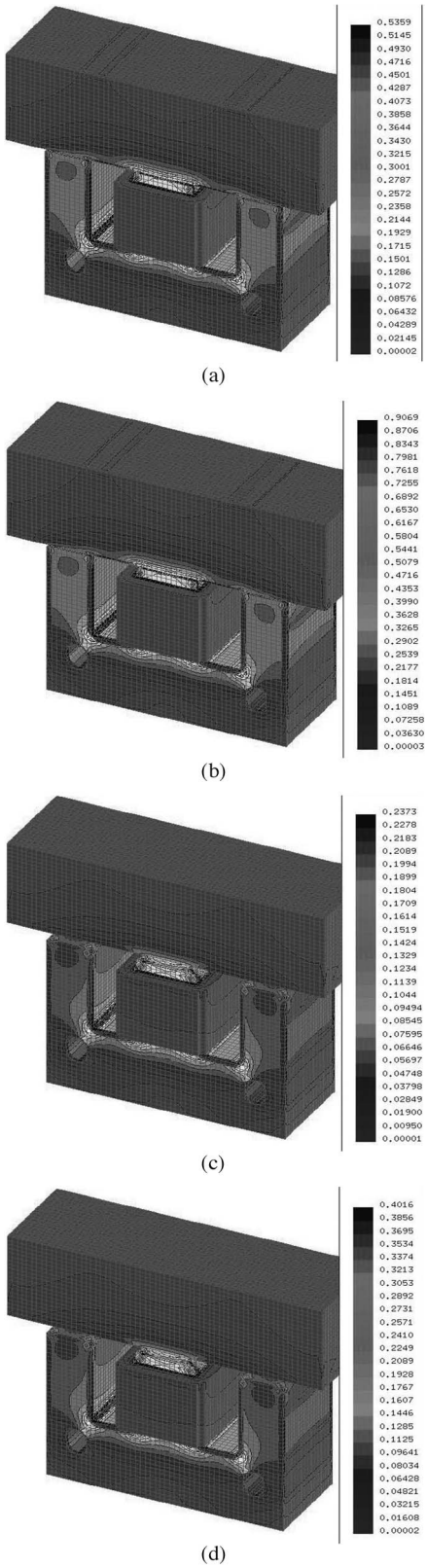

Fig. 11. (a) Flux contours: $z = 0.5$ mm, $i = 6.5$ A. (b) Flux contours: $z = 0.5$ mm, $i = 11$ A. (c) Flux contours: $z = 2$ mm, $i = 6.5$ A. (d) Flux contours: $z = 2$ mm, $i = 11$ A.

V. Actual Performance and Results Analysis

The block diagram of the force measurement experimental setup is shown in Fig. 13. A dSPACE DS1103 DSP board that is plugged into an ISA bus of a Pentium 4 computer executes all control functions. The current is implemented by a commercial analog amplifier driver.

The force measurement installation is shown in Fig. 14. The installation consists of two round poles embedded in the base of the structure with one supporting pole that can be moved up and down and one connector. The installation is fixed on the body of the motor. The levitation coil is fixed on the connector and is limited to move in the vertical direction by the two round poles. The air gap can be changed by adjusting the supporting pole's position. A load cell is fixed on the supporting pole and

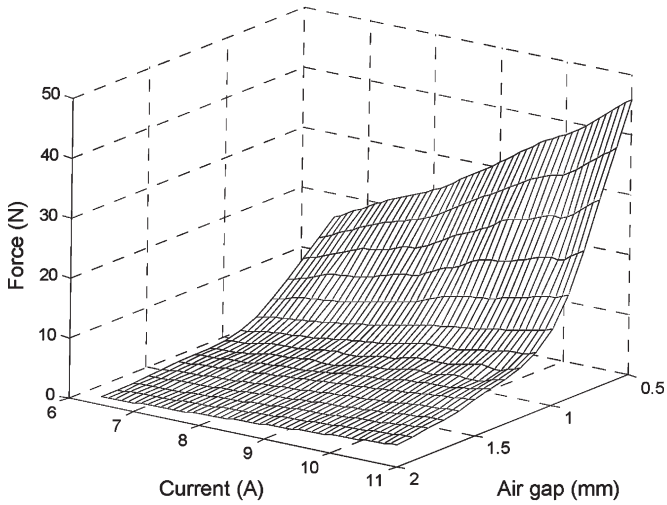

Fig. 12. FEA force–current–position 3-D chart.

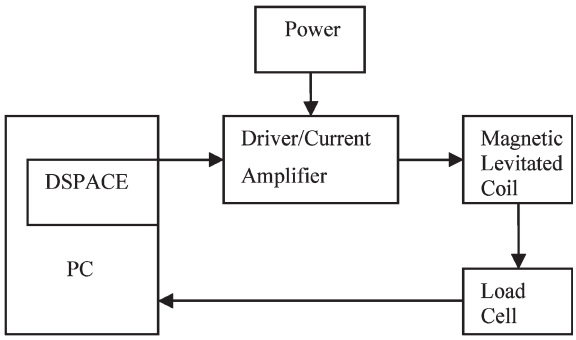

Fig. 13. Block diagram of experimental setup for force measurement.

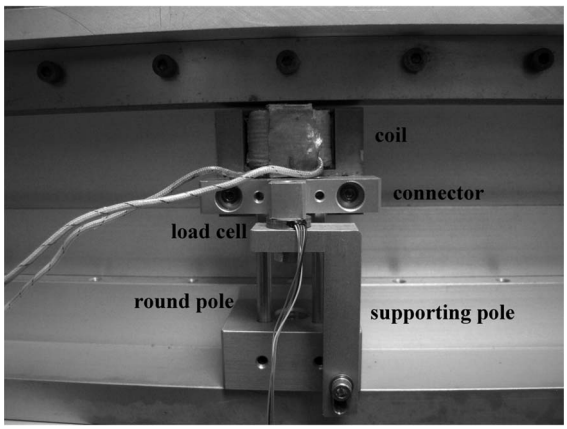

Fig. 14. Force measurement installation.

the connector to measure the levitation force. The measured levitation force profile at different current excitation levels and air gaps is shown in Fig. 15.

The same force variation trend can be found between the MCA model, the FEA model, and the experimental model from the results of force distribution in Figs. 8, 12 and 15. The further levitation force comparison is illustrated as shown in Fig. 16.

According to Fig. 16, the nonlinear characteristics of the levitation force are demonstrated. It can be seen that the levitation force abruptly increases when the air gap is less than 1 mm. This

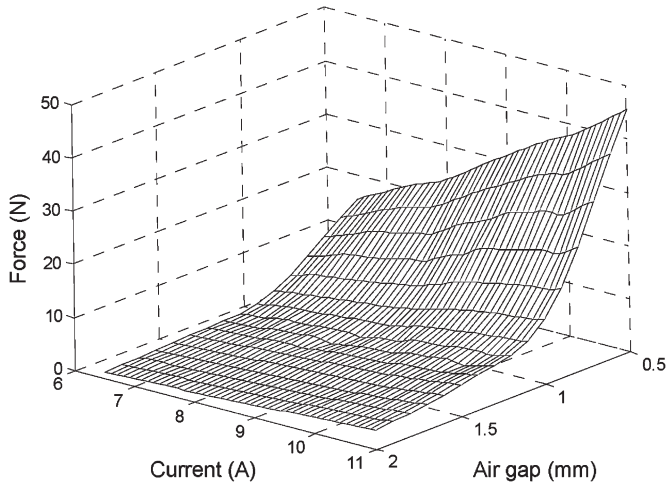

Fig. 15. Experimental force–current–position 3-D chart.

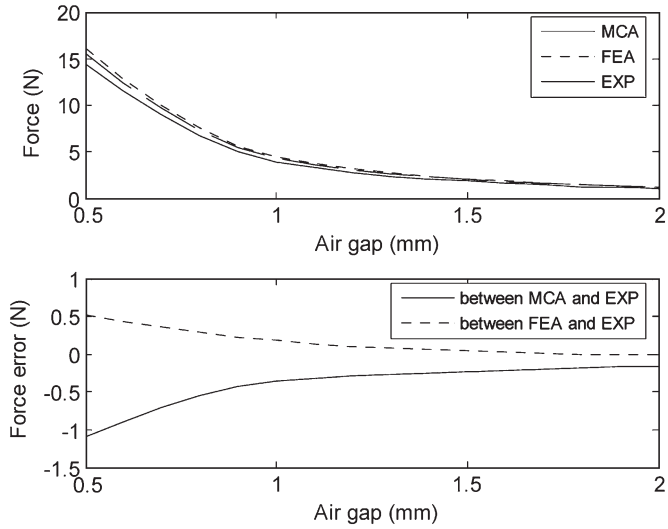

Fig. 16. Force comparison with $I = 6.5$ A.

suggests that higher efficient levitation force can be obtained by restricting the air gap within a small air gap.

Fig. 16 and Table III give the force comparison and the force error when the exciting current is 6.5 A. As the findings in Fig. 16 reveal, the estimated force from the FEA model is a little bit larger than the measured force, the estimated force from the MCA model is a little bit less than the measured force, and the force error between the FEA model and experiment is less than that between the MCA model and experiment. For example, as shown in Table III, when the air gap is 0.5 mm, the error between the FEA and experiment is 3.61%, whereas the error between the MCA and experiment is 6.58%; when the air gap is 2 mm, the error between the FEA and experiment is 2.46%, whereas the error between the MCA and experiment is 9.84%. For reasons of simple and rapid calculation, there are only seven main flux paths considered in the MCA model. While the FEA method simulates the levitation system by mesh discretization, there are much more paths considered in the FEA model. As a result, the total flux and the levitation force computed from the MCA model is less than that from the FEA model. There are two possible explanations for the force error

TABLE III
FORCE VALUES AND RELATIVE ERRORS WHEN $I = 6.5$ A

Air gap	MCA	FEA	EXP	Improved MCA (IMCA)	MCA /EXP	FEA /EXP	IMCA /EXP
0.5mm	14.48 N	16.06 N	15.50 N	15.03 N	6.58%	3.61%	3.03%
1mm	3.92 N	4.41 N	4.26 N	4.07 N	7.98%	3.52%	4.46%
1.5mm	1.89 N	2.11 N	2.07 N	1.99 N	8.70%	1.93%	3.86%
2mm	1.10 N	1.25 N	1.22 N	1.26 N	9.84%	2.46%	3.28%

between the FEA model and experiment. One reason is that there is energy loss in the measurement. Another reason is that slight mechanical friction exists, although the round poles are smooth. Consequently, the measured force is a little less than the estimated force from the FEA model.

Table III also reveals that the accuracy of the FEA model is ahead that of the MCA model, and errors between the MCA and experiment become aggravating when the air gap enlarges. Noting that the air gap is not a fixed value, from Fig. 11, the 3-D FEA flux contours simulation, and we find that the configuration of flux path in the air gap changes with the increase in air gap. Therefore, the parameter t in the MCA model should not be a fixed but an adjustable value according to the air gap. Supposing that $\alpha = k(z/h)$, where k is a constant gain, let $t = (h/12)\alpha$; then, the parameter t will change and adhere to the air gap, and the MCA model is improved on the basis of the 3-D FEA model. The force value and error of the improved MCA model are listed in Table III when the current is 6.5 A. When the air gap is 0.5 mm, the force error is meliorated from 6.58% to 3.03% after using the improved MCA model; when the air gap is 2 mm, the force error is meliorated from 9.84% to 3.28%. It can be seen from Table III that the result of the improved MCA model is very close to that of the FEA model.

Although the FEA model is an accurate simulation tool, the solution period needed is a great disadvantage to the FEA model. MCA calculation is implemented by MATLAB software; according to a fixed air gap and a given current, the force computing time is about 3 s, and forces with different air gaps and currents can be conveniently calculated by changing the numerical values of the air gap and current. In contrast with the MCA model, excluding the model generation and meshes, according to a fixed air gap and a given current, the force calculating time for the 3-D FEA model is not less than 1 min, owing to the large number of nodes. In the process of operating the FEA software, the meshing time is relative to the user's skill, particularly for some local regions needing refinement mesh, e.g., the air gap region. Generally, considering the meshing time, the calculating time for the 3-D FEA model is around 20 min. Furthermore, the space of air gap needs to be meshed again if the air gap is changed, and it will be time consuming for the 3-D FEA model, compared with the MCA model.

From the comparisons between the MCA, FEA, and experiment, it can be seen that the results of the improved MCA are very close to those of the FEA, and both are approximate to those of experiment. This agreement demonstrates the effectiveness of simulation models for the design of the proposed magnetic levitated actuator.

VI. CONCLUSION

A novel magnetic levitated switched reluctance linear actuator system has been proposed in this paper. There is no permanent magnet required in the proposed actuator; therefore, the total cost can be reduced. Moreover, this proposed actuator can operate in harsh environmental conditions, such as high temperature.

The magnetic levitated system is basically composed of an LSRM and four magnetic levitation coils. In this paper, both the MCA model and the 3-D FEA model have been applied to analyze the force of the levitation coils. Corresponding force measurements have also been performed in the proposed system. The MCA method can be used to quickly and approximately calculate the electromagnetic force, and the accuracy of the MCA model is improved on the basis of the FEA model. The results of the improved MCA model are very close to those of the FEA model, and the agreement of both the method results with the measurement results verifies the feasibility of the two simulation models. These results provide useful information for the mechanical structure design of the magnetic levitated linear switched reluctance actuator.

REFERENCES

[1] T. Azukizawa, M. Morishita, S. Kanda, N. Tamura, and T. Yokoyama, "A linear induction motor control system for magnetically levitated carrier system," *IEEE Trans. Veh. Technol.*, vol. 38, no. 2, pp. 102–108, May 1989.

[2] K. Venkataratnam and A. B. Chattopadhyay, "Analysis of electromagnetic forces in a levitated short rotor LIM. I—Finite length and finite width effects," *IEEE Trans. Energy Convers.*, vol. 17, no. 1, pp. 95–106, Mar. 2002.

[3] K. Venkataratnam and A. B. Chattopadhyay, "Analysis of electromagnetic forces in a levitated short rotor LIM. II—Lateral stabilization," *IEEE Trans. Energy Convers.*, vol. 17, no. 1, pp. 102–106, Mar. 2002.

[4] K. Komori and T. Yamane, "Magnetically levitated micro PM motors by two types of active magnetic bearings," *IEEE/ASME Trans. Mechatronics*, vol. 6, no. 1, pp. 43–49, Mar. 2001.

[5] P. Karutz, T. Nussbaumer, W. Gruber, and J. W. Kolar, "Novel magnetically levitated two-level motor," *IEEE/ASME Trans. Mechatronics*, vol. 13, no. 6, pp. 658–668, Dec. 2008.

[6] K. Nagashima, Y. Iwasa, K. Sawa, and M. Murakami, "Controlled levitation of bulk superconductors," *IEEE Trans. Appl. Supercond.*, vol. 10, no. 3, pp. 1642–1648, Sep. 2000.

[7] Z. Makni, M. Besbes, and C. Marchand, "Multiphysics design methodology of permanent-magnet synchronous motors," *IEEE Trans. Veh. Technol.*, vol. 56, no. 4, pp. 1524–1530, Jul. 2007.

[8] C. S. Edrington, M. Krishnamurthy, and B. Fahimi, "Bipolar switched reluctance machines: A novel solution for automotive applications," *IEEE Trans. Veh. Technol.*, vol. 54, no. 3, pp. 795–808, May 2005.

[9] X. D. Xue, K. W. E. Cheng, J. K. Lin, Z. Zhang, K. F. Luk, T. W. Ng, and N. C. Cheung, "Optimal control method of motoring operation for SRM drives in electric vehicles," *IEEE Trans. Veh. Technol.*, vol. 59, no. 3, pp. 1191–1204, Mar. 2010.

[10] H. C. Roters, *Electromagnetic Devices*, 1st ed. New York: Wiley, 1941, pp. 130–139.

[11] H. D. Chai, "Permeance model and reluctance force between toothed structures," in *Proc. 2nd Annu. Symp. Incremental Motion Control Syst. Device*, May 1973, pp. 141–153.

[12] R. Krishnan, *Switched Reluctance Motor Drives: Modeling, Simulation, Analysis, Design, and Applications*, 1st ed. Boca Raton, FL: CRC, 2001, pp. 138–141.

[13] U. S. Deshpande, J. J. Cathy, and E. Richter, "High-force density linear switched reluctance machine," *IEEE Trans. Ind. Appl.*, vol. 31, no. 2, pp. 345–351, Mar./Apr. 1995.

[14] N. K. Sheth and K. R. Rajagopal, "Calculation of flux-linkage characteristics of a switched reluctance motor by flux tube method," *IEEE Trans. Magn.*, vol. 41, no. 10, pp. 4069–4071, Oct. 2005.
[15] W. Meyer, D. Bucherl, and H. G. Herzog, "High speed magnetic network solving," in *Proc. IEEE Int. Elect. Mach. Drives Conf.*, Miami, FL, May 2009, pp. 529–534.
[16] T. S. Low, H. Lin, and S. X. Chen, "Analysis and comparison of switched reluctance motors with different physics sizes using a 2D finite element method," *IEEE Trans. Magn.*, vol. 31, no. 6, pp. 3503–3505, Nov. 1995.
[17] A. di Gaeta, L. Glielmo, V. Giglio, and G. Police, "Modeling of an electromechanical engine valve actuator based on a hybrid analytical–FEM approach," *IEEE/ASME Trans. Mechatronics*, vol. 13, no. 6, pp. 625–637, Dec. 2008.
[18] H. C. Lai, D. Rodger, and P. J. Leonard, "Coupled meshes in 3D problems involving movements," *IEEE Trans. Magn.*, vol. 28, no. 2, pp. 1732–1734, Mar. 1992.
[19] A. Benhama, A. C. Williamson, and A. B. J. Reece, "Force and torque computation from 2-D and 3-D finite element field solutions," *Proc. Inst. Elect. Eng.—Elect. Power Appl.*, vol. 146, no. 1, pp. 25–31, Jan. 1999.
[20] F. Ishibashi, S. Noda, and M. Mochizuki, "Numerical simulation of electromagnetic vibration of small induction motors," *Proc. Inst. Elect. Eng.—Elect. Power Appl.*, vol. 145, no. 6, pp. 528–534, Nov. 1998.
[21] A. Arkkio, M. Antila, K. Pokki, A. Simon, and E. Lantto, "Electromagnetic force on a whirling cage rotor," *Proc. Inst. Elect. Eng.—Elect. Power Appl.*, vol. 147, no. 5, pp. 353–360, Sep. 2000.
[22] M. Popescu, D. M. Ionel, T. J. E. Miller, S. J. Dellinger, and M. I. McGilp, "Improved finite element computations of torque in brushless permanent magnet motors," *Proc. Inst. Elect. Eng.—Elect. Power Appl.*, vol. 152, no. 2, pp. 271–276, Mar. 2005.
[23] W. C. Gan and N. C. Cheung, "Development and control of a low-cost linear variable-reluctance motor for precision manufacturing automation," *IEEE/ASME Trans. Mechatronics*, vol. 8, no. 3, pp. 326–333, Sep. 2003.
[24] P. J. Leonard, H. C. Lai, and R. J. H. Cottingham, "Treatment of symmetry in three dimensional finite element models of machines coupled to external circuits," *IEEE Trans. Energy Convers.*, vol. 14, no. 4, pp. 1276–1281, Dec. 1999.
[25] P. K. Vong, H. C. Lai, and D. Rodger, "Optimization of electromagnetic devices using parameterized templates," *IEEE Trans. Magn.*, vol. 37, no. 5, pp. 3538–3541, Sep. 2001.
[26] *User Manual, MEGA V6.29*, Appl. Electromagn. Res. Centre, Univ. Bath, London, U.K., Aug. 4, 2003.

Zhen Gang Sun (S'08) received the B.Sc. and M.Sc. degrees from South China University of Technology, Guangzhou, China, in 2000 and 2003, respectively. He is currently working toward the Ph.D. degree with the Department of Electrical Engineering, Hong Kong Polytechnic University, Kowloon, Hong Kong.

His research interests are motion control and magnetic levitation machines.

Norbert C. Cheung (S'85–M'91–SM'05) received the B.Sc. degree from the University of London, London, U.K., the M.Sc. degree from the University of Hong Kong, Kowloon, Hong Kong, and the Ph.D. degree from the University of New South Wales, Sydney, Australia, in 1981, 1987, and 1995, respectively.

He is currently with the Department of Electrical Engineering, Hong Kong Polytechnic University, Kowloon. His research interests are motion control, actuator design, and power electronic drives.

Dr. Cheung is a Chartered Engineer in the U.K. and a member of the Institution of Engineering and Technology, U.K.

Shi Wei Zhao (S'07–M'09) received the B.Sc. degree from Central South University, Changsha, China, the M.Sc. degree from South China University of Technology, Guangzhou, China, and the Ph.D. degree from Hong Kong Polytechnic University, Kowloon, Hong Kong, in 2000, 2003, and 2008, respectively.

He is currently a Postdoctoral Fellow with the Department of Electrical Engineering, Hong Kong Polytechnic University. His research interests are motion control and machine drives.

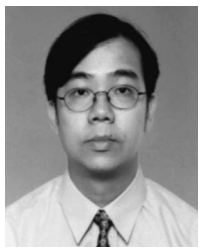

Wai-Chuen Gan (S'94–M'02–SM'06) received the B.Eng. degree in electronic engineering and the M.Phil. and Ph.D. degrees in electrical and electronic engineering from Hong Kong University of Science and Technology, Hong Kong, in 1995, 1997, and 2001, respectively.

From 1997 to 1999, he was a Motion Control Application Engineer with ASM Assembly Automaton Ltd., Hong Kong. He rejoined the same company in 2002, where he is responsible for the development of linear switched reluctance motor systems for semiconductor assembly equipment. His current research interests include robust control of ac machines, power electronics, and the design and control of linear switched reluctance motors.